ACS OMEGA

Article

Cite This: ACS Omega 2019, 4, 3850−3859

http://pubs.acs.org/journal/acsodf

Water Splitting Reaction at Polar Lithium Niobate Surfaces

Christof Dues,[†,‡] Wolf Gero Schmidt,[¶] and Simone Sanna*[,†,‡]

[†]Institut für Theoretische Physik and [‡]Center for Materials Research (LaMa), Justus-Liebig-Universität Gießen, Heinrich-Buff-Ring 16, 35392 Gießen, Germany

[¶]Department Physik, Universität Paderborn, Warburger Str. 100, 33098 Paderborn, Germany

ABSTRACT: Water splitting is a highly promising, environmentally friendly approach for hydrogen production. It is often discussed in the context of carbon dioxide free combustion and storage of electrical energy after conversion to chemical energy. Since the oxidation and reduction reactions are related to significant overpotentials, the search for suitable catalysts is of particular importance. Ferroelectric materials, for example, lithium niobate, attracted considerable interest in this respect. Indeed, the presence of surfaces with different polarizations and chemistries leads to spatial separation of reduction and oxidation reactions, which are expected to be boosted by the electrons and holes available at the positive and negative surfaces, respectively. Employing the density functional theory and a simplified thermodynamic approach, we estimate the overpotentials related to the oxygen evolution reaction (OER) and hydrogen evolution reaction (HER) on both polar $LiNbO_3$ (0001) surfaces. Our calculations performed for ideal surfaces in vacuum predict the lowest overpotential for the hydrogen evolution reaction (0.4 V) and for the oxygen evolution reaction (1.2 V) at the positive and at the negative surfaces, respectively, which are lower than (or comparable with) commonly employed catalysts. However, calculations performed to model the aqueous solution in which the reactions occur reveal that the presence of water substantially increases the required overpotential for the HER, even inverting the favorable polarization direction for oxidation and reduction reactions. In aqueous solution, we predict an overpotential of 1.2 V for the HER at the negative surface and 1.1 V for the OER at the positive surface.

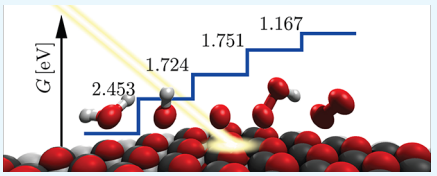

INTRODUCTION

Hydrogen production is a promising way to convert excess electrical power to chemical energy. Once produced, hydrogen can be combusted by engines, reconverted into electricity by fuel cells and stored in large caverns. After methanation (reaction of hydrogen with carbon oxides to methane, CH_4), it can be readily used as natural gas, for which extended infrastructures (cars, heating, etc.) already exist.

Water splitting $2H_2O \rightarrow 2H_2 + O_2$ is a feasible way to produce hydrogen. Water is largely available, easy to handle, and directly provides ready to use molecular H_2 with only O_2 as the by-product. As a redox reaction, water splitting consists of the reduction reaction $4H^+ + 4e^- \rightarrow 2H_2$ and the oxidation reaction $2H_2O \rightarrow O_2 + 4H^+ + 4e^-$, which produce hydrogen and oxygen, respectively. They are correspondingly abbreviated as HER (hydrogen evolution reaction) and OER (oxygen evolution reaction). The latter is the more complex reaction, as four electrons have to be transferred. The reaction is furthermore characterized by large activation barriers (i.e., large contributions to the overpotential), which inhibit its course. At this point begins the search of a suitable catalyst, which makes the water splitting faster and more efficient.

Water splitting is achieved by different approaches. Instead of providing the required energy with an electrical source, Fujishima et al. showed that hydrogen can be produced on TiO_2 surfaces under irradiation of sunlight.[1] This approach does not require an external electrical potential and can make hydrogen an abundant energy source. Similar ideas exist for artificial photosynthesis and other catalytic processes.[2] Photochemical water splitting on nonpolar GaN surfaces has been thoroughly investigated combining ab initio molecular dynamics and time-dependent density functional theory simulations.[3,4]

Another way to efficiently achieve water splitting exploits ferroelectric substrates. Hong et al. made use of the piezoelectrochemical effect of ZnO microfibers and $BaTiO_3$ microdendrites to generate hydrogen and oxygen via direct water decomposition,[5] while Kakekhani and Ismail-Beigi designed a catalytic cycle for water splitting that employs the pyroelectric effect in ferroelectric $PbTiO_3$.[6]

Ferroelelectrics, for example, lithium niobate ($LiNbO_3$, LN), offer promising properties for photocatalytic water splitting. These materials are characterized by an internal polarization. To compensate for the polarization charges, surfaces orthogonal to the polar direction modify their morphology and stoichiometry,[7−10] resulting in two distinct terminations with different chemical properties[11−15] (Figure 1). This largely compensates the polarization charge[16−19] reducing the surface electric field. Ferroelectric substrates provide different advantages for photocatalytic water splitting. On the one hand, incident radiation (with energy larger than the LN band gap of 3.78 eV[20,21]) produces electron−hole-pairs, which show an enhanced lifetime, as the electric field hinders their recombination. On the other hand, reduction and oxidation

Received: November 23, 2018
Accepted: January 25, 2019
Published: February 21, 2019

DOI: 10.1021/acsomega.8b03271
ACS Omega 2019, 4, 3850−3859

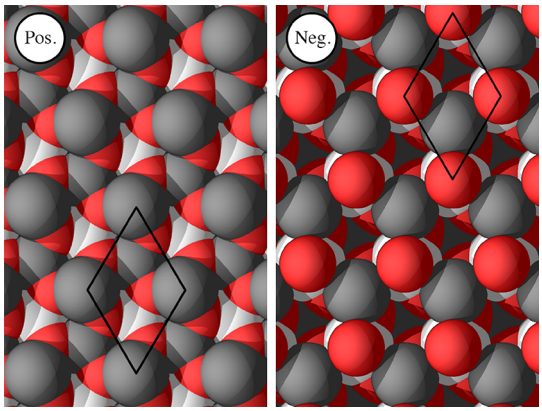

Figure 1. (0001) (positive, left-hand side) and (000$\bar{1}$) (negative, right-hand side) surfaces of $LiNbO_3$. Red, gray, and white spheres denote oxygen, lithium, and niobium atoms, respectively. The 1 × 1 surface unit cell is indicated by black lines.

reactions occur on spatially separated surfaces, which hinders the recombination of the products.[22] Furthermore, the positive surface (electron doped) is expected to provide the electrons necessary for the HER, while the negative surface (hole doped) is expected to collect the excess electrons resulting from the OER. Both effects are suitable to catalysis; indeed, lithium niobate has been proposed as a promising substrate for photocatalytic reactions.[23] In the case of artificial photosynthesis, a similar redox reaction under solar irradiation, Stock and Dunn showed experimentally that the catalytic efficiency of TiO_2 is outperformed by the one of $LiNbO_3$.[24] This makes large quantum efficiencies expectable.

For this reason, we investigate both parts of the water splitting reaction on the polar surfaces of $LiNbO_3$. To describe the system of surface and reagents, we employ the density functional theory. A simplified thermodynamical approach is used to determine Gibbs free energy profiles for a prototypical reaction mechanism, which ultimately allows us to estimate the overpotential of both reactions on either surfaces. In the first step, we demonstate the catalytic effect of ferroelectric surfaces by modeling the reactions in vacuum and on ideal surfaces. Overpotentials as low as 0.39 and 1.22 V are calculated for the HER and OER, respectively, which are comparable to theoretical values estimated for excellent catalysts such as rutile RuO_2 and TiO_2 surfaces.[25,26] In the second step, we model the water splitting reaction under more realistic conditions, that is, the model influence of the aqueous solution on the surface reactions. The presence of water substantially enhances the overpotentials necessary to drive the reaction and even inverts the favored polarization direction for OER and HER, thus hindering the water splitting reaction under experimental conditions. The investigation of the relative position of reaction potentials and substrate band edges shows that the positive surface is a very good catalyst for the HER, while the negative surface cannot efficiently drive the OER.

METHODS AND MODELS

Density Functional Theory. To describe the electronic structure on the atomic level from first principles, we make use of the density functional theory as implemented in VASP (Version 5.3.5).[27,28] Thus, we model the structures and total energies of clean and adsorbed LN surfaces in a supercell description. To this end, we employ PAW potentials[29] that include the $1s^1$, $2s^1$, $2s^22p^4$, and $4s^24p^64d^45s^1$ valence electrons in the case of H, Li, O, and Nb, respectively. The basis set contains plane waves with kinetic energy up to 400 eV. The integration in the reciprocal space is performed on a 2 × 2 × 1 Monkhorst−Pack grid, which reflects the symmetry of the supercell.[30] Convergence tests show that neither larger basis sets nor denser *k*-meshes result in an improved description.[a] To provide consistency with previous investigations of $LiNbO_3$, we choose the PW91 description of the exchange correlation potential.[31] The same argument holds for the choice of the DFT-D2 functional by Grimme et al.[32] to describe dispersion interactions at the surface.

Table 1 shows the influence of the van der Waals functional on the absorption energies and the adsorption distance of H_2O

Table 1. H_2O on the Negative LN Surface: Comparison of Adsorption Energy and Bond Length between the Outmost Li Atom of the Surface Termination and the Molecule's O Calculated Using Different Dispersion Functionals

dispersion functional	ref	E_{ads} (eV)	$d(\mathrm{Li}, \mathrm{O}^{H_2O})$ (Å)
none		−1.003	1.886
DFT-D2	33	−1.201	1.873
DFT-D3	32	−1.157	1.878
DFT-D3 (BJ)	34	−1.172	1.875
TS	35	−1.246	1.877
TS (iHP)	36, 37	−1.126	1.878
TS (SCS)	38	−1.186	1.879
dDsC	39, 40	−1.152	1.876
optPBE-vdW	41−44	−1.161	1.899
optB88-vdW	41−44	−1.169	1.893
optB86b-vdW	41−44	−1.153	1.887
vdW-DF2	42−45	−1.152	1.899

molecules calculated exemplarily at the negative surface of LN. All the functionals result in an enhanced adsorption energy, showing that van der Waals forces substantially contribute to the bonding between H_2O and the substrate. The choice of a more recent functional is expected to give similar results.

Surface calculations within periodic boundary conditions are performed by inclusion of a vacuum layer of 20 Å, which strongly reduces the interaction between different periodic images. The length of the vacuum layer ensures energy differences between different adsorption configurations to be converged within 1 meV. Due to the magnitude of the vacuum layer, the effect of dipole corrections[46,47] is minor and amounts to, for example, 10^{-4} eV for the H_2O adsorption energy.

Three $LiNbO_3$ trilayers of LN *Z*-cut, the surface termination, and all adsorbates sit on top of three fixed trilayers of LN, which model the bulk material. Making use of the conjugate gradient algorithm, the relaxation of atoms is performed until the Hellmann−Feynman forces are smaller than 0.02 eV/Å. The total energy of molecules in the gas phase is calculated in a supercell with dimensions of 10 × 11 × 12 $Å^3$, using the Γ-point for the reciprocal space sampling. This procedure allows to reproduce the adsorption energies of a previous study,[14] which are given by

$$E_{ads} = E^{tot}(\mathrm{Ads@Slab}) - E^{tot}(\mathrm{Slab}) - E^{tot}(\mathrm{Ads}) \quad (1)$$

A negative sign in the adsorption energy indicates the adsorbed state being preferred over the nonadsorbed state. Adsorption energies are calculated using a 1 × 1 surface unit cell, which yields adsorption energies converged within 15

DOI: 10.1021/acsomega.8b03271
ACS Omega 2019, 4, 3850−3859

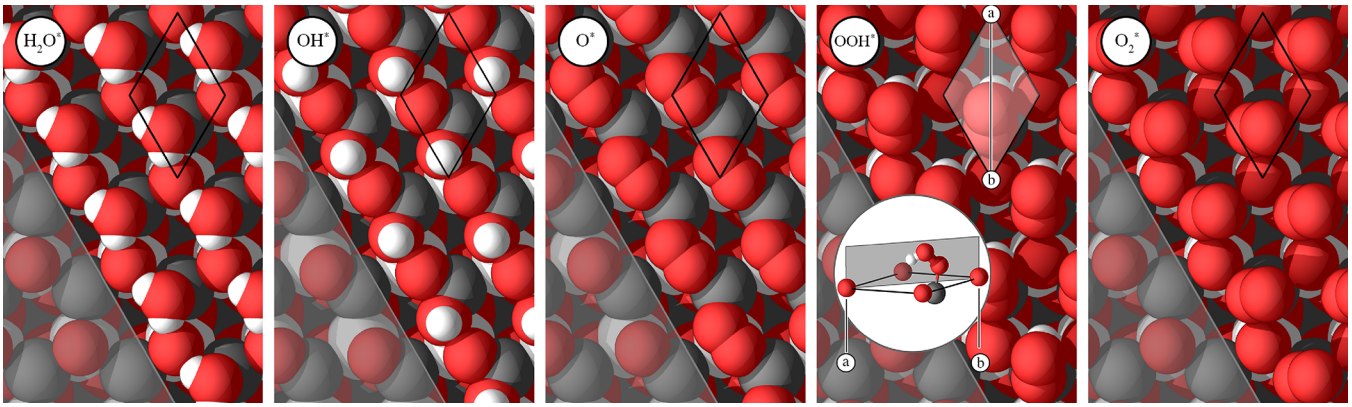

Figure 2. Adsorbates in reactions A–D adsorbed at the negative LN surface. From left to right, H_2O*, OH*, O*, OOH*, and O_2*. Color coding as in Figure 1. Small white spheres denote hydrogen atoms. The surface unit cell is indicated by black lines. The adsorbates are hidden in the gray shaded area to highlight adsorption-induced structural changes. The OOH* has a tilted structure shown in the inset (the location of the gray plane is indicated by the a–b line).

meV with respect to a 2 × 2 or a 3 × 3 surface unit cell, which yield the same value. The adsorption configurations are determined either on the basis of previous results[11,14] or by testing different adsorption geometries.

Potential energy surfaces (PESs) for the adsorption of different molecules or fragments are calculated constraining the lateral coordinates of the oxygen atom of the adsorbate and allowing the remaining degrees of freedom to relax. We have thereby evaluated the adsorption energy on a rectangular mesh for 56 possible positions.

To model water-covered $LiNbO_3$ (0001) surfaces, we consider the effect of water on the substrate. It is known that H_2O enhances the $LiNbO_3$ surface roughness.[14] Furthermore, in a water environment, the positively polarized surface (electron doped) tends to attract OH^-, while the negatively polarized surface (hole doped) attracts H^+. Thus, we qualitatively model the aqueous environment by placing water fragments on the perfect $LiNbO_3$ surfaces. The water fragments are placed according to the configurations we have determined in a previous investigation.[11] Although this approach represents a crude approximation that does not allow for a quantitative estimate of the overpotentials, it represents a step toward more realistic conditions and allows a qualitative description of the effect of the aqueous environment. We want to remark that our approach includes further simplifications that may lead to deviations from real systems. Apart from the mentioned water fragments, we model the ideal surfaces of lithium niobate without nanodomains, defects, dislocations, and impurities, occurring in real samples. They might provide highly active catalytic sites, enhancing the efficiency of perfect surfaces. We simulate the reactions with a solid–gas model, which does involve neither partial or multiple coverage nor the coexistence of different adsorbates. Solvation effects are omitted as well.

Thermodynamic Approach. The description of chemical reactivity involves the estimation of the energy barrier corresponding to a chemical reaction (influencing a reaction's time constant) and the energy difference between products and educts. The relevant thermodynamic potential for chemical reactions is the Gibbs free energy $G(p,T)$. Its differences during a reaction can be calculated in the theory by Nørskov et al.[48] by means of

$$\Delta G = \Delta E^{\mathrm{tot}} - T\Delta S + \Delta E^{\mathrm{ZPE}} + \Delta G_U + \Delta G_{\mathrm{pH}} \quad (2)$$

including the terms

$$\Delta G_U = -e{\cdot}U \qquad \Delta G_{\mathrm{pH}} = -k_B T \ln(10){\cdot}\mathrm{pH}$$

to correct differences in Gibbs free energy due to the application of an electric potential or a different pH value. ΔE^{tot}, $T\Delta S$, and ΔE^{ZPE} denote the differences in DFT total energies, entropic contributions, and zero-point energies, respectively. The latter two terms determine the contributions to free energy $F(T,V)$, which are not included in E^{tot}. While an additional summand $p{\cdot}V$ is still needed to convert $F(T,V)$ to Gibbs free energy, its influence at realistic pressures is very small and thus negligible.[49] Additionally, we neglect the entropic contributions to eq 2. Their influence at metal oxide surfaces has been shown to be small, for example, at RuO_2 (110) surfaces for different oxygen partial pressures[9] and at TiO_2 (110) surfaces for the OER.[25] Furthermore, this term is expected to be of similar magnitude for both LN (0001) orientations, and we focus here on the difference between differently polarized surfaces. Therefore, we calculate reaction energy differences in a simplified fashion as

$$\Delta G \approx \Delta E^{\mathrm{tot}} + \Delta G_U + \Delta G_{\mathrm{pH}} \quad (3)$$

In this way, the computational effort is reduced and systems of the size investigated in this work become accessible. This approach has proven to be more suitable than traditional ways to include neglected terms that tend "to use oversimplified treatments of entropic contributions".[50] A change of the pH value or of the potential influences the Gibbs free energies and equilibrium potentials equally.[51] Therefore, the overpotential is not dependent on those terms.

Within Nørskov's framework, coupled proton–electron transfers (CPET) are considered. Furthermore, we employ the "numerical" hydrogen electrode as reference, meaning that the reaction

$$H_2 \rightleftharpoons 2(H^+ + e^-)$$

is in equilibrium, and its Gibbs free energy difference is $\Delta G = 0$ by definition. Consequently, the energy of proton–electron pairs in subsequent reaction pathways can be accounted for via $E^{\mathrm{tot}}(H^+ + e^-) = \frac{1}{2}E^{\mathrm{tot}}(H_2)$. The overpotential η is estimated for the OER by the difference between the largest ΔG and the commonly accepted water (to oxygen) oxidation potential to be 1.23 eV.[52] In the case of the HER, the overpotential

DOI: 10.1021/acsomega.8b03271
ACS Omega 2019, 4, 3850–3859

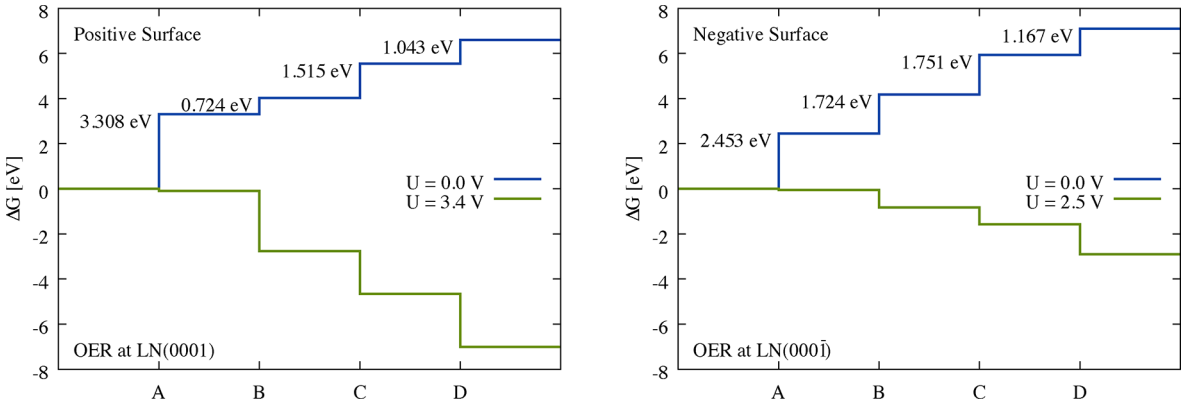

Figure 3. Comparison of Gibbs free energy profile for the OER at the pristine polar LN surfaces. The horizontal axis depicts reactions A–D. Evaluating eq 3 with zero overpotential or minimal necessary overpotential results in the blue and green curves, respectively.

corresponds to the largest ΔG, as the corresponding potential is by definition 0.00 eV.

RESULTS

OER. We investigate the OER of the water splitting reaction using the "associative" reaction mechanism[48,53] (reactions A–D) as the model reaction. Other reaction pathways are possible.[54] However, their investigation exceeds the scope of this paper. The oxidation reaction is assumed to have a peroxide intermediate OOH adsorbed to the surface.[25] As pointed out by Valdés et al.,[25] the recombination of two adjacent oxygen atoms is associated with a large activation barrier.[55] X* denotes molecule X adsorbed at the surface.

$$H_2O^* \rightarrow OH^* + H^+ + e^- \quad (A)$$

$$OH^* \rightarrow O^* + H^+ + e^- \quad (B)$$

$$H_2O + O^* \rightarrow OOH^* + H^+ + e^- \quad (C)$$

$$OOH^* \rightarrow O_2^* + H^+ + e^- \quad (D)$$

Following the approach outlined in the previous section, we determine the adsorption geometry of each molecule (Figure 2) and calculate the energy difference between each step at both the positive and the negative LN surfaces. For each surface, the results are depicted by the blue lines in Figure 3. Reaction A is associated with the largest energy difference, which therefore determines the overpotential η. The overpotentials on the positive and negative surfaces amount to 2.08 and 1.22 eV, respectively. Finally, the application of a bias voltage with the potential required to overcome the largest energy difference makes the reaction possible as depicted by the green lines in Figure 3. The required potential is larger on the positive surface than on the negative surface, which makes the OER more feasible for the latter surface.

The calculated overpotential of 1.22 V for the OER at the LN (000$\bar{1}$) surface is comparable with the values calculated for excellent catalysts such as Pt (111) (1.32 V[53]), s-triazene based graphitic carbon nitride (0.93 V[52]), and rutile TiO_2 (110) (0.78 V[25]) or RuO_2 (110) (0.64 V[26]). However, while for rutile such values are achieved for surfaces fully covered with oxygen or for strongly defective surfaces, the values calculated for $LiNbO_3$ correspond to defect-free non-precovered surfaces. The catalytic activity of the clean surfaces is thus not related to surface modifications but is an inherent surface property, which might be further enhanced by nanoscale structuring or chemical treatment.

HER. The HER, which is the reduction of protons to molecular hydrogen, is somewhat simpler. The transfer processes of two electrons must be considered.

$$* + H^+ + e^- \rightarrow H^* \quad (E)$$

$$H^* + H^+ + e^- \rightarrow H_2^* \quad (F)$$

Again, the adsorption geometries (shown in Figure 4) and afterward the Gibbs free energy profiles are determined

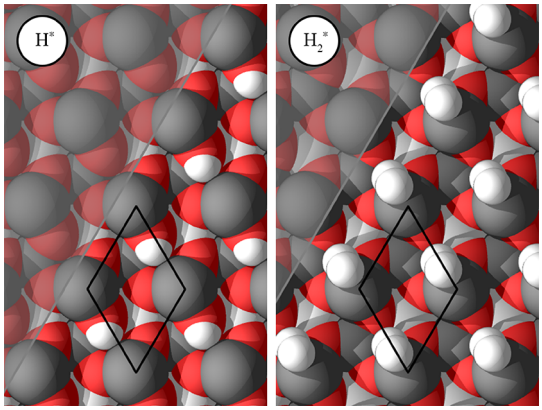

Figure 4. Adsorbates in reactions E and F adsorbed at the positive LN surface: H* (left-hand side) and H_2* (right-hand side). Color coding as in Figure 2. The surface unit cell is indicated by black lines. The adsorbates are hidden in the gray shaded area to highlight adsorption-induced structural changes.

(Figure 5). The blue lines show the case of no external bias voltage. The adsorption of the first hydrogen atom results in the rate-determining step with the largest energy difference for both surfaces. The adsorption of the second hydrogen atom is associated with a negative energy difference, indicating a spontaneous reaction progression. The difference in the Gibbs free energy profiles of the entire HER process (i.e., before and after reactions E and F) corresponds to the H_2 adsorption energy, which represents the difference in the adsorption energies of educts and products. This has been verified by explicitly calculationg the H_2 adsorption energy.

Choosing the numerical hydrogen electrode as the reference potential allows to express the difference in Gibbs free energy by means of the difference in adsorption energy. Thus, the

DOI: 10.1021/acsomega.8b03271
ACS Omega 2019, 4, 3850–3859

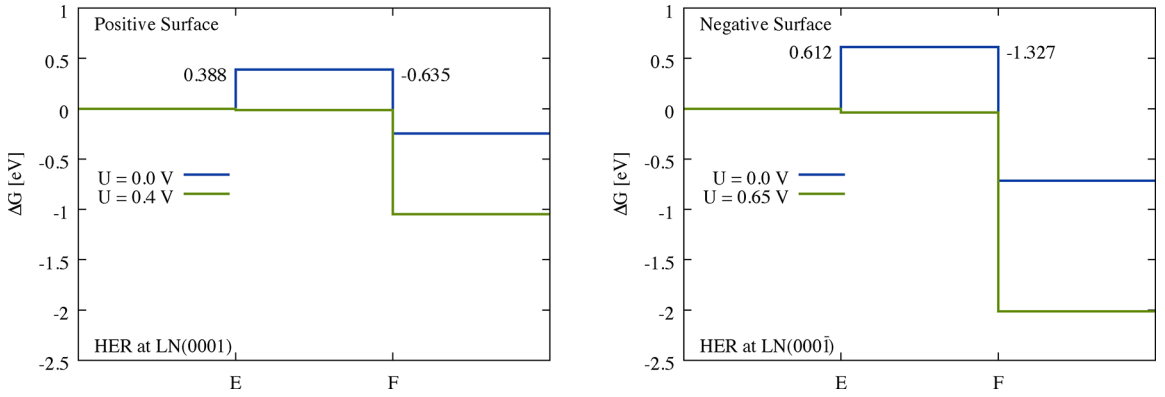

Figure 5. Comparison of Gibbs free energy profile for the HER at the clean polar LN surfaces. The horizontal axis represents the reaction coordinate according to reactions E and F. Evaluating eq 3 with zero overpotential or minimal necessary overpotential results in the blue and green curves, respectively. The Gibbs free energy difference of the entire HER in the case of zero bias voltage corresponds to the H_2 adsorption energy.

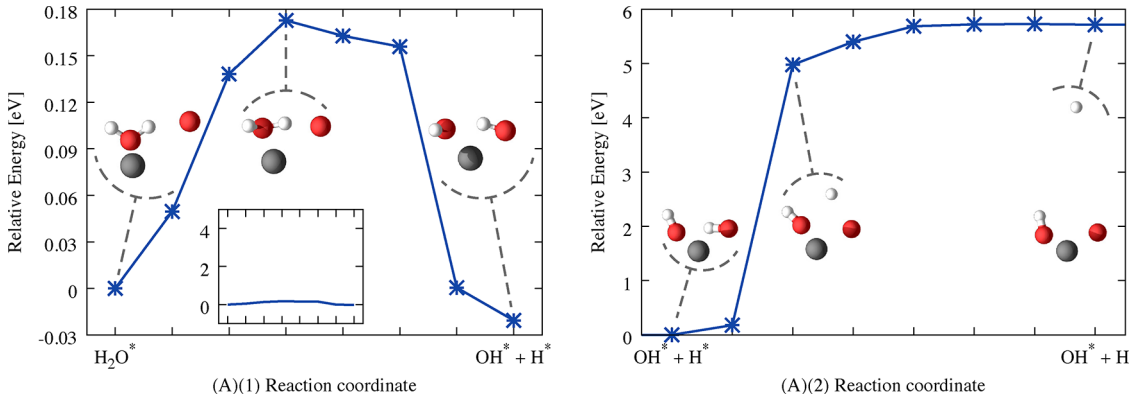

Figure 6. Minimum energy paths derived from reaction A divided into a dissociation part (left-hand side) and a desorption part (right-hand side). Insets depict the atomic geometry for selected points along the MEP, showing the top view (left figure) or the side view (right figure) of the outmost Li−O termination and the adsorbates (color coding as in Figure 2). An additional inset on the left-hand side displays the barrier at the same energy scale as in the right figure.

overpotential on the positive surface is 0.39 eV, while we get a value of 0.61 eV for the negative surface. The HER is more feasible on the positive LN surface due to the smaller overpotential and becomes exoenergetic by application of an external voltage of about 0.4 eV (green lines in Figure 5).

The calculated overpotential for the HER is noticeable. On the one hand, its very low value makes the pristine LN (0001) surface an excellent catalyst. For comparison, the HER overpotential calculated for s-triazene based graphitic carbon nitride amounts to 0.82 V.[52] On the other hand, this value is rather different from the overpotential needed for the OER. Even if remarkable, this difference must not be surprising, as differently polarized $LiNbO_3$ surfaces are known to be morphologically and chemically very different.

Energy Barrier. The results concerning OER and HER shown in Figures 3 and 5 give only a partial picture of the energetics of reactions A−F. Energy barriers may indeed separate the intermediate reactions. To further investigate this issue, we employ the nudged elastic band (NEB) method to get an insight into the energy landscape. We make use of six images that are initially equidistantly distributed along the reaction coordinate that transforms the state of an absorbed H_2O^* and the state of dissociative adsorption OH* + H* in the multidimensional configuration space. This is the first part or step A in reaction A. The calculated barrier represents the energy potential that must be overcome by H_2O from a metastable adsorption mode to a more stable mode, which is the dissociative adsorption known for other polar oxides.[56] This interpolation has been done carefully to exclude an artificial translation of molecules along the surface to equivalent adsorption sites (from rotational or translational symmetry). The result after convergence to the minimum energy path (MEP) is shown in the left-hand side of Figure 6. Although the final state is even lower in energy by about 0.02 eV, a barrier of nearly 0.18 eV has to be overcome. The saddle point in the configuration space is characterized by a 90° rotation of the water molecule around one hydrogen−oxygen bond, with the other hydrogen atom pointing out of the surface plane. The first hydrogen points to the oxygen atom of the surface termination (due to a hydrogen bond), which moves approximately 0.48 Å toward the hydrogen atom. In the final state, the separated hydrogen atom bonds to the oxygen of the surface termination. The barrier is quite small compared to the energy differences calculated in the previous section. It is only about 7% of the Gibbs free energy difference of reaction A. We can thus conclude that energy barriers do not have a substantial effect on the reaction kinetics of this step.

We investigate a second reaction path that describes the second step of reaction A, the removal of a hydrogen atom beginning from the final state of the last pathway (OH* + H* → OH* + H), and makes reaction A complete. We want to remark that this is not the barrier associated with the

DOI: 10.1021/acsomega.8b03271
ACS Omega 2019, 4, 3850−3859

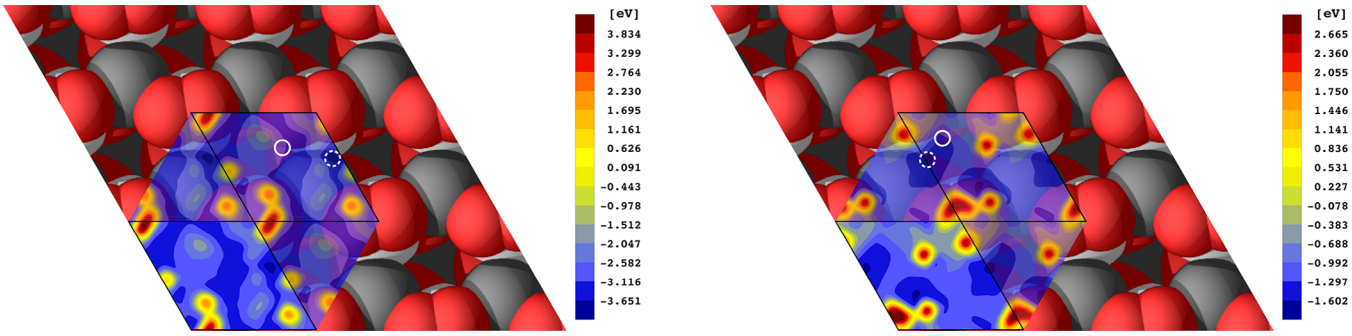

Figure 7. PESs showing favorable and unfavorable adsorption sites for OH (left-hand side) and H_2O (right-hand side) on the negative LN surface precovered with O*. Color coding as in Figure 1. The solid and the dashed circles in each PES correspond to adsorption scenarios (a) and (b) described in the main text, respectively.

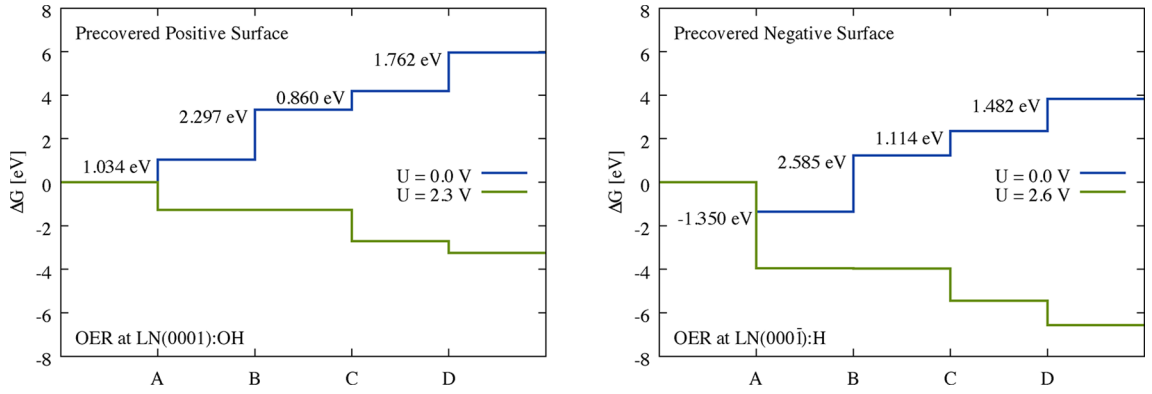

Figure 8. Comparison of Gibbs free energy profile for the OER at the polar LN surfaces modified to account for aqueous conditions. The horizontal axis depicts the reaction coordinate according to reactions A–D. Evaluating eq 3 with zero overpotential or minimal necessary overpotential results in the blue and green curves, respectively.

deprotonation. The latter is the energy needed by H^+ to go to the solvent via the collective effect of H_2O molecules nearby. As the desorption of H^+ occurs only by the help of dative bonding from nearby water molecules, which are absent in our model, the deprotonation barrier would not be accessible within our approach. We rather test whether removing an hydrogen from the surface requires overcoming an energy barrier. The H atom is considered as separated from the surface when its distance from the topmost surface atom is higher than 6 Å. At that distance, the interaction energy becomes negligible. The result is presented in the right-hand side of Figure 6. The corresponding MEP does not have a saddle point, that is, an energy corresponding exactly to the difference between initial and final state that is necessary for the removal of the hydrogen. In the configuration space, the hydrogen moves mostly perpendicular to the surface, while the remaining surface results in the geometry of OH* (see Figure 2). Also, the energy difference between the initial and final state compares well to the first reaction's Gibbs free energy difference after subtracting the energy corresponding to the removed hydrogen. The largest contribution to the overpotential is thus due to the interaction of H and the LN surface in this step rather than to the stability of the H_2O molecule itself.

In conclusion, the water splitting reactions on clean $LiNbO_3$ surfaces are not hindered by additional energy barriers beyond the energy difference between the distinct adsorption configurations.

Secondary Water Adsorption. The presence of a large energy barrier makes the recombination of O* + O* → O_2* unlikely.[55] This results in the formation of an unusual OOH* peroxide complex by integration of a second water molecule in the third CPET (reaction C). This CPET can occur either before or after the interaction of secondary H_2O molecules with O*. Thus, either a deprotonation (of H_2O) with subsequent adsorption OH + O* → OOH* or an adsorption H_2O + O* → H_2O_2* with subsequent deprotonation may occur. Which reaction path actually occurs is still a matter of debate. This question is of rather general nature, as it also arises considering alternative reaction paths.

We address this open question for the water splitting reaction on $LiNbO_3$. Therefore, we calculate the PES of the adsorption of H_2O and OH on the precovered surface. We restrict the investigation to the negative surface, where the OER is more likely to occur. We define the position of the adsorbate by keeping the lateral coordinates of the corresponding oxygen atom constant. All other degrees of freedom are relaxed. The energy landscape plots are shown in Figure 7.

Two main different adsorption geometry scenarios are predicted: (a) The second molecule (either H_2O or OH) adsorbs on the surface and interacts with the already adsorbed oxygen atom to build the peroxide complex. (b) The second molecule adsorbs on the surface without interacting with the already adsorbed oxygen (e.g., due to the lateral distance), and the peroxide complex is not formed. Other adsorption

DOI: 10.1021/acsomega.8b03271
ACS Omega 2019, 4, 3850–3859

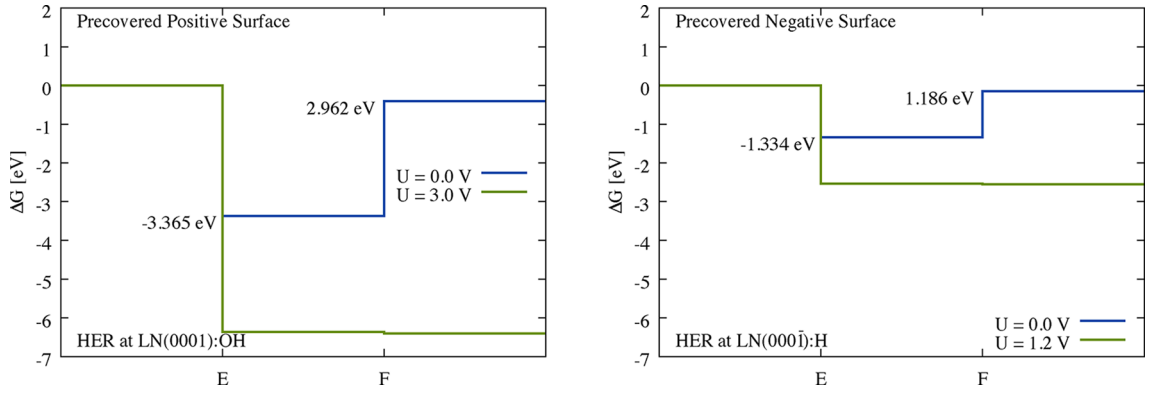

Figure 9. Comparison of Gibbs free energy profile for the HER at the polar LN surfaces modified to account for aqueous conditions. The horizontal axis represents the reaction coordinate according to reactions E and F. Evaluating eq 3 with zero overpotential or minimal necessary overpotential results in the blue and green curves, respectively. The Gibbs free energy difference of the entire HER in the case of zero bias voltage corresponds to the H_2 adsorption energy.

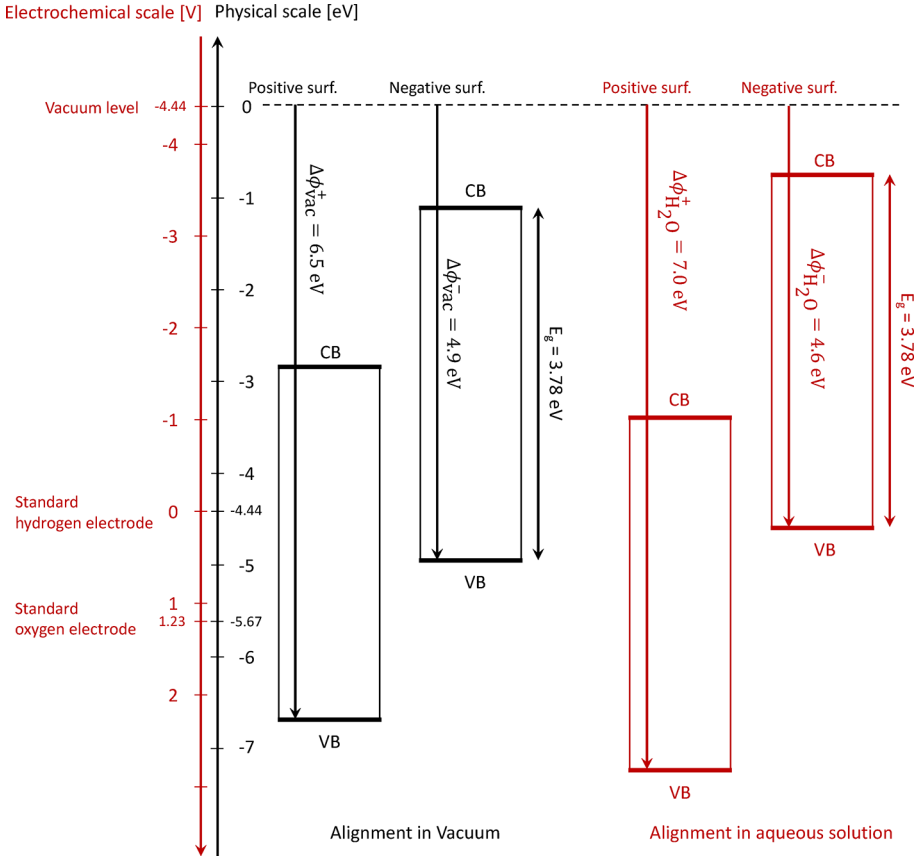

Figure 10. Band positions of $LiNbO_3$ in vacuum (black lines) and in aqueous solutions (red lines) in relation to the redox reactions of water splitting. The relative electrode potentials are converted into electronic energies following the standard convention for aqueous systems.[60]

configurations characterized by large adsorption energies are not further discussed.

In the case of OH as an adsorbate, the global minimum of the PES (represented by a dashed circle on the left-hand side of Figure 7) corresponds to an energy of −3.65 eV and an adsorption geometry of scenario (b), which does not result in the assumed peroxide intermediate. The lowest point on the energy landscape, where OOH is built, is denoted by the solid circle. This point is associated with an energy of −2.79 eV, which is less favorable by 0.86 eV.

In the case of H_2O as an adsorbate instead, the global minimum (−1.60 eV) corresponds to a type (b) adsorption geometry, while the type (a) scenario (energy of −1.34 eV) is energetically less favorable by 0.26 eV. In summary, we conclude that the formation of the OOH peroxide complex is easier after adsorption of H_2O than of OH and the CPET takes place after H_2O adsorption.

HER and OER in Aqueous Solution. Ferroelectric surfaces have a diverging electrostatic surface energy due to the presence of a nonzero dipole moment on all the unit cells throughout the material.[57] Different mechanisms occur to reduce the electrostatic instability. While inner compensation mechanisms such as surface relaxation and reconstructions (both considered in our models) take place in UHV, external

DOI: 10.1021/acsomega.8b03271
ACS Omega 2019, 4, 3850−3859

compensation mechanisms such as the adsorption of molecules and fragments available from the environment might further contribute to compensate the polarization charges at ambient conditions. This might deeply modify the surface chemistry. In particular, in a water environment, the positively polarized surface (electron doped) tends to become OH^- terminated, while the negatively polarized surface (hole doped) becomes H^+ terminated. Thus, LN surfaces under experimental conditions might differ from the previously discussed pristine LN surfaces. To verify the effect of the aqueous solution on the water splitting reaction, we model water-covered $LiNbO_3$ surfaces as described in the Methods and Models.

The results are shown in Figures 8 and 9. They demonstrate that the water splitting reaction at the $LiNbO_3$ ferroelectric surfaces under experimentally relevant conditions is very different from the idealized situation modeling clean surfaces. The presence of water levels and substantially raises the overpotentals needed to drive the reactions and even inverts the favorable surface for the OER and HER. The smallest overpotential for HER in aqueous conditions is found at the negative surface and amounts to 1.2 V [for clean surfaces, it was 0.4 V at the LN (0001)], while the smallest overpotential for OER amounts to 1.1 V, substantially the same value as for pristine surfaces, however, at the positive surface. The low overpotential for the OER at the positive surface of different catalysts in aqueous conditions has been explained by the enhanced oxygen availability, due to the presence of the OH fragments.

The calculated values suggest that ferroelectric $LiNbO_3$ surfaces under experimental conditions still have a catalytic function; however, the expected efficiency is not higher than that reported, for example, for rutile. This explains why excellent catalytic performances are only obtained for $LiNbO_3$ nanowires or finely milled crystals,[24,58] while the bulk counterpart does not show an outstanding catalytic efficiency.

Band Alignment. To achieve water splitting, the catalyst must be able to drive the HER and the OER. In particular, the conduction band must be located above the HER potential, so that (photo)excited electrons from the conduction band can take part to the lower lying HER reaction. Also, the valence band must be located below the OER potential so that holes from the valence band may become available for the OER. Shortly, the reaction potentials must be inside the $LiNbO_3$ band edges.

Figure 10 compares the potential of the valence and conduction bands of $LiNbO_3$ with the potentials of the oxidation of water and hydrogen reduction located as previously discussed at 1.23 and 0.00 V, respectively (Figure 10, left-hand side). This corresponds in the more common absolute scale (Figure 10, right-hand side) to −5.67 and −4.44 eV. To determine the position of the $LiNbO_3$ band edges on this scale, we use the ionization energy $\Delta\Phi$, which corresponds to the energy necessary to bring an electron from the valence band edge to infinity (vacuum level). Concerning clean surfaces (black lines in Figure 10), both measurements[59] and calculations[8] estimate the ionization potentials to $\Delta\Phi^+ = 6.5$ eV for the positive and $\Delta\Phi^- = 4.9$ eV for the negative surface, respectively. This marks the position of the valence band in the absolute scale. Assuming a band gap of 3.78 eV, the conduction band is placed at −2.72 eV (−1.12 eV) for the positive (negative) surface. Thus, the oxidation and reduction potentials are within the band gap in the case of the positive surface, while only the hydrogen reaction potential is within the $LiNbO_3$ band gap. Considering the overpotentials, the positive surface can efficiently drive the HER, but the valence band holes at the negative surface cannot oxidize water. Although it does not mean that the reaction will not take place,[b] this fact strongly reduces the catalytic efficiency of LN ideal surfaces.

The presence of water modifies the ionization energy and thus the relative position of the vacuum level and band edges.[14] As a consequence of the adsorbate-to-surface electron transfer at the positive surface, the work function is increased by roughly 0.49 eV at the positive surface, while it is reduced by 0.34 eV at the negative surface, as a consequence of the surface-to-adsorbate electronic charge transfer. The new band alignment is shown in the right part of Figure 10 (red lines). Although the band shift is not negligible, it does not drastically modify the situation described for pristine surfaces. While the positive surface remains a very good catalyst for the HER (and also for the OER, which becomes feasible in the water environment), the negative surface cannot efficiently drive the OER.

CONCLUSIONS

This manuscript presents density functional based simulations of the water splitting on clean ferroelectric LN surfaces and in aqueous solution, calculated by model OER and HER mechanisms following the theory by Nørskov et al.[48]

In the case of clean surfaces, the oxidation (reduction) reaction has the lowest overpotential on the negative (positive) surface and is therefore more likely to proceed. This fits perfectly to the picture that the spontaneous polarization of ferroelectric materials drives photogenerated charge carriers to the polar surfaces (electrons to the positive, holes to the negative surface), making injection or removal of electrons easier than in less chemically strained systems. Using the NEB method, we ruled out that additional reaction barriers hinder the first reaction steps, which determine the overpotential on LN surfaces. The secondary water adsorption was analyzed by means of potential energy maps, which indicate that the adsorption of a water molecule prior to the deprotonation is more likely to happen than vice versa.

Under experimental conditions (i.e., in aqueous solution), the calculated overpotentials are substantially higher than in UHV, representing a serious constraint for the catalytic efficiency of $LiNbO_3$ crystals. Furthermore, contrary to the water splitting on clean surfaces, the OER is favored at the positive surface and the HER at the negative surface. It seems that the water-covered LN (0001) surfaces are too stable in the investigated neutral case to lead to an efficient water splitting. This explains why the observed outstanding catalytic activity of $LiNbO_3$ is only achieved for nanostructured or finely milled samples,[58] where step edges and defects may provide catalytically active sites.

The determination of the active sites efficiently catalyzing the water splitting reaction will be the crucial goal for future investigations, as it may allow to produce tailored structures of large surface area with high density of active sites. Similarly, further work has to be dedicated to band engineering. Substituting Nb cations (e.g., with Ta or further transition metals), it might be possible to tailor the band edges. Tuning the position of the latter with respect to the standard oxygen and hydrogen potentials, the OER at the negative surface could become possible. Combining the knowledge about active

DOI: 10.1021/acsomega.8b03271
ACS Omega 2019, 4, 3850−3859

catalytic sites and band alignment, highly efficient $LiNbO_3$-based catalyst for water splitting might be designed.

AUTHOR INFORMATION

Corresponding Author

*E-mail: simone.sanna@theo.physik.uni-giessen.de.

ORCID

Simone Sanna: 0000-0003-4416-0252

Notes

The authors declare no competing financial interest.

ACKNOWLEDGMENTS

The Deutsche Forschungsgemeinschaft (DFG) is gratefully acknowledged for financial support via projects TRR142, FOR1700, SCHM161/21 and SCHM1361/25. The Höchstleistungrechenzentrum Stuttgart (HLRS) is gratefully acknowledged for grants of high-performance computer time. We acknowledge computational resources provided by the HPC Core Facility and the HRZ of the Justus-Liebig-Universität Gießen and by the Paderborn Center for Parallel Computing (PC^2).

ADDITIONAL NOTES

[a]A 40 eV rise of cutoff energy results in a total energy difference of 50 meV; the difference between a 4 × 4 × 1 grid and the chosen one is smaller than 0.3 meV.
[b]$LiNbO_3$'s conduction band electrons are highly reducing and can reduce water fragments, allowing different reaction pathways.[24]

REFERENCES

(1) Fujishima, A.; Honda, K. Electrochemical Photolysis of Water at a Semiconductor Electrode. *Nature* **1972**, *238*, 37−38.
(2) Kakekhani, A.; Ismail-Beigi, S. Polarization-driven catalysis via ferroelectric oxide surfaces. *Phys. Chem. Chem. Phys.* **2016**, *18*, 19676−19695.
(3) Shen, X.; Small, Y. A.; Wang, J.; Allen, P. B.; Fernandez-Serra, M. V.; Hybertsen, M. S.; Muckerman, J. T. Photocatalytic Water Oxidation at the GaN $(10\bar{1}0)$-Water Interface. *J. Phys. Chem. C* **2010**, *114*, 13695−13704.
(4) Akimov, A. V.; Muckerman, J. T.; Prezhdo, O. V. Nonadiabatic Dynamics of Positive Charge during Photocatalytic Water Splitting on GaN(10-10) Surface: Charge Localization Governs Splitting Efficiency. *J. Am. Chem. Soc.* **2013**, *135*, 8682−8691.
(5) Hong, K.-S.; Xu, H.; Konishi, H.; Li, X. Direct Water Splitting Through Vibrating Piezoelectric Microfibers in Water. *J. Phys. Chem. Lett.* **2010**, *1*, 997−1002.
(6) Kakekhani, A.; Ismail-Beigi, S. Ferroelectric oxide surface chemistry: water splitting via pyroelectricity. *J. Mater. Chem. A* **2016**, *4*, 5235−5246.
(7) Sanna, S.; Gavrilenko, A. V.; Schmidt, W. G. Ab initio investigation of the $LiNbO_3$ (0001) surface. *Phys. Status Solidi C* **2010**, *7*, 145−148.
(8) Sanna, S.; Schmidt, W. G. Lithium niobate *X*-cut, *Y*-cut, and *Z*-cut surfaces from ab initio theory. *Phys. Rev. B* **2010**, *81*, 214116.
(9) Sanna, S.; Berth, G.; Hahn, W.; Widhalm, A.; Zrenner, A.; Schmidt, W. G. Localised Phonon Modes at $LiNbO_3$ (0001) Surfaces. *Ferroelectrics* **2011**, *419*, 1−8.
(10) Sanna, S.; Dues, C.; Schmidt, W. G. Modeling atomic force microscopy at $LiNbO_3$ surfaces from first-principles. *Comput. Mater. Sci.* **2015**, *103*, 145−150.
(11) Hölscher, R.; Sanna, S.; Schmidt, W. G. Adsorption of OH and H at the $LiNbO_3$ (0001) surface. *Phys. Status Solidi C* **2012**, *9*, 1361−1365.
(12) Rode, S.; Hölscher, R.; Sanna, S.; Klassen, S.; Kobayashi, K.; Yamada, H.; Schmidt, W. G.; Köhnle, A. Atomic-resolution imaging of the polar $(000\bar{1})$ surface of $LiNbO_3$ in aqueous solution by frequency modulation atomic force microscopy. *Phys. Rev. B* **2012**, *86*, 075468.
(13) Riefer, A.; Sanna, S.; Schmidt, W. G. Polarization-dependent methanol adsorption on lithium niobate Z-cut surfaces. *Phys. Rev. B* **2012**, *86*, 125410.
(14) Sanna, S.; Hölscher, R.; Schmidt, W. G. Polarization-dependent water adsorption on the $LiNbO_3$ (0001) surface. *Phys. Rev. B* **2012**, *86*, 205407.
(15) Hölscher, R.; Schmidt, W. G.; Sanna, S. Modeling $LiNbO_3$ Surfaces at Ambient Conditions. *J. Phys. Chem. C* **2014**, *118*, 10213−10220.
(16) Sanna, S.; Rode, S.; Hölscher, R.; Klassen, S.; Marutschke, C.; Kobayashi, K.; Yamada, H.; Schmidt, W. G.; Kühnle, A. Charge compensation by long-period reconstruction in strongly polar lithium niobate surfaces. *Phys. Rev. B* **2013**, *88*, 115422.
(17) Sanna, S.; Hölscher, R.; Schmidt, W. G. Temperature dependent $LiNbO_3$ (0001): Surface reconstruction and surface charge. *Appl. Surf. Sci.* **2014**, *301*, 70−78.
(18) Johann, F.; Soergel, E. Quantitative measurement of the surface charge density. *Appl. Phys. Lett.* **2009**, *95*, 232906.
(19) Jungk, T.; Hoffmann, Á.; Soergel, E. Detection mechanism for ferroelectric domain boundaries with lateral force microscopy. *Appl. Phys. Lett.* **2006**, *89*, No. 042901.
(20) Thierfelder, C.; Sanna, S.; Schindlmayr, A.; Schmidt, W. G. Do we know the band gap of lithium niobate? *Phys. Status Solidi C* **2010**, *7*, 362−365.
(21) Riefer, A.; Friedrich, M.; Sanna, S.; Gerstmann, U.; Schindlmayr, A.; Schmidt, W. G. $LiNbO_3$ electronic structure: Many-body interactions, spin-orbit coupling, and thermal effects. *Phys. Rev. B* **2016**, *93*, No. 075205.
(22) Sanna, S.; Schmidt, W. G. $LiNbO_3$ surfaces from a microscopic perspective. *J. Phys.: Condens. Matter* **2017**, *29*, 413001.
(23) Liu, G.; You, S.; Ma, M.; Huang, H.; Ren, N. Removal of Nitrate by Photocatalytic Denitrification Using Nonlinear Optical Material. *Environ. Sci. Technol.* **2016**, *50*, 11218−11225.
(24) Stock, M.; Dunn, S. $LiNbO_3$- A new material for artificial photosynthesis. *IEEE Trans. Ultrason., Ferroelectr., Freq. Control* **2011**, *58*, 1988−1993.
(25) Valdés, Á.; Qu, Z.-W.; Kroes, G.-J.; Rossmeisl, J.; Nørskov, J. K. Oxidation and Photo-Oxidation of Water on TiO_2 Surface. *J. Phys. Chem. C* **2008**, *112*, 9872−9879.
(26) Wirth, J.; Monturet, S.; Klamroth, T.; Saalfrank, P. Adsorption and (photo-) electrochemical splitting of water on rutile ruthenium dioxide. *EPL* **2011**, *93*, 68001.
(27) Kresse, G.; Furthmüller, J. Efficient iterative schemes for ab initio total-energy calculations using a plane-wave basis set. *Phys. Rev. B* **1996**, *54*, 11169−11186.
(28) Kresse, G.; Furthmüller, J. Efficiency of ab-initio total energy calculations for metals and semiconductors using a plane-wave basis set. *Comput. Mater. Sci.* **1996**, *6*, 15−50.
(29) Blöchl, P. E. Projector augmented-wave method. *Phys. Rev. B* **1994**, *50*, 17953−17979.
(30) Monkhorst, H. J.; Pack, J. D. Special points for Brillouin-zone integrations. *Phys. Rev. B* **1976**, *13*, 5188−5192.
(31) Perdew, J. P.; Chevary, J. A.; Vosko, S. H.; Jackson, K. A.; Pederson, M. R.; Singh, D. J.; Fiolhais, C. Atoms, molecules, solids, and surfaces: Applications of the generalized gradient approximation for exchange and correlation. *Phys. Rev. B* **1992**, *46*, 6671−6687.
(32) Grimme, S.; Antony, J.; Ehrlich, S.; Krieg, H. A consistent and accurate ab initio parametrization of density functional dispersion correction (DFT-D) for the 94 elements H-Pu. *J. Chem. Phys.* **2010**, *132*, 154104.
(33) Grimme, S. Semiempirical GGA-type density functional constructed with a long-range dispersion correction. *J. Comput. Chem.* **2006**, *27*, 1787−1799.

DOI: 10.1021/acsomega.8b03271
ACS Omega 2019, 4, 3850−3859

(34) Grimme, S.; Ehrlich, S.; Goerigk, L. Effect of the damping function in dispersion corrected density functional theory. *J. Comput. Chem.* **2011**, *32*, 1456−1465.
(35) Tkatchenko, A.; Scheffler, M. Accurate Molecular Van Der Waals Interactions from Ground-State Electron Density and Free-Atom Reference Data. *Phys. Rev. Lett.* **2009**, *102*, No. 073005.
(36) Bučko, T.; Lebègue, S.; Hafner, J.; Ángyán, J. G. Improved Density Dependent Correction for the Description of London Dispersion Forces. *J. Chem. Theory Comput.* **2013**, *9*, 4293−4299.
(37) Bučko, T.; Lebègue, S.; Ángyán, J. G.; Hafner, J. Extending the applicability of the Tkatchenko-Scheffler dispersion correction via iterative Hirshfeld partitioning. *J. Chem. Phys.* **2014**, *141*, No. 034114.
(38) Tkatchenko, A.; DiStasio, R. A., Jr.; Car, R.; Scheffler, M. Accurate and Efficient Method for Many-Body van der Waals Interactions. *Phys. Rev. Lett.* **2012**, *108*, 236402.
(39) Steinmann, S. N.; Corminboeuf, C. A generalized-gradient approximation exchange hole model for dispersion coefficients. *J. Chem. Phys.* **2011**, *134*, No. 044117.
(40) Steinmann, S. N.; Corminboeuf, C. Comprehensive Benchmarking of a Density-Dependent Dispersion Correction. *J. Chem. Theory Comput.* **2011**, *7*, 3567−3577.
(41) Klimeš, J.; Bowler, D. R.; Michaelides, A. Chemical accuracy for the van der Waals density functional. *J. Phys.: Condens. Matter* **2010**, *22*, No. 022201.
(42) Dion, M.; Rydberg, H.; Schröder, E.; Langreth, D. C.; Lundqvist, B. I. Van der Waals Density Functional for General Geometries. *Phys. Rev. Lett.* **2004**, *92*, 246401.
(43) Román-Pérez, G.; Soler, J. M. Efficient Implementation of a van der Waals Density Functional: Application to Double-Wall Carbon Nanotubes. *Phys. Rev. Lett.* **2009**, *103*, No. 096102.
(44) Klimeš, J.; Bowler, D. R.; Michaelides, A. Van der Waals density functionals applied to solids. *Phys. Rev. B* **2011**, *83*, 195131.
(45) Lee, K.; Murray, E. D.; Kong, L.; Lundqvist, B. I.; Langreth, D. C. Higher-accuracy van der Waals density functional. *Phys. Rev. B* **2010**, *82*, No. 081101.
(46) Neugebauer, J.; Scheffler, M. Adsorbate-substrate and adsorbate-adsorbate interactions of Na and K adlayers on Al(111). *Phys. Rev. B* **1992**, *46*, 16067−16080.
(47) Bengtsson, L. Dipole correction for surface supercell calculations. *Phys. Rev. B* **1999**, *59*, 12301−12304.
(48) Nørskov, J. K.; Rossmeisl, J.; Logadottir, A.; Lindqvist, L.; Kitchin, J. R.; Bligaard, T.; Jónsson, H. Origin of the Overpotential for Oxygen Reduction at a Fuel-Cell Cathode. *J. Phys. Chem. B* **2004**, *108*, 17886−17892.
(49) Reuter, K.; Scheffler, M. Composition, structure, and stability of RuO_2(110) as a function of oxygen pressure. *Phys. Rev. B* **2001**, *65*, No. 035406.
(50) Nørskov, J. K.; Abild-Pedersen, F.; Studt, F.; Bligaard, T. Density functional theory in surface chemistry and catalysis. *Proc. Natl. Acad. Sci. U. S. A.* **2011**, *108*, 937−943.
(51) Valdés, Á.; Brillet, J.; Grätzel, M.; Gudmundsdóttir, H.; Hansen, H. A.; Jónsson, H.; Klüpfel, P.; Kroes, G.-J.; Formal, F. L.; Man, I. C.; et al. Solar hydrogen production with semiconductor metal oxides: new directions in experiment and theory. *Phys. Chem. Chem. Phys.* **2012**, *14*, 49−70.
(52) Srinivasu, K.; Ghosh, S. K. Photocatalytic splitting of water on s-triazine based graphitic carbon nitride: an ab initio investigation. *J. Mater. Chem. A* **2015**, *3*, 23011−23016.
(53) Rossmeisl, J.; Logadottir, A.; Nørskov, J. K. Electrolysis of water on (oxidized) metal surfaces. *Chem. Phys.* **2005**, *319*, 178−184.
(54) Matsumoto, Y.; Sato, E. Electrocatalytic properties of transition metal oxides for oxygen evolution reaction. *Mater. Chem. Phys.* **1986**, *14*, 397−426.
(55) Nørskov, J. K.; Bligaard, T.; Logadottir, A.; Bahn, S.; Hansen, L. B.; Bollinger, M.; Bengaard, H.; Hammer, B.; Sljivancanin, Z.; Mavrikakis, M.; et al. Universality in Heterogeneous Catalysis. *J. Catal.* **2002**, *209*, 275−278.
(56) Ranea, V. A.; Schneider, W. F.; Carmichael, I. DFT characterization of coverage de- pendent molecular water adsorption modes on α-Al_2O_3(0001). *Surf. Sci.* **2008**, *602*, 268−275.
(57) Noguera, C. Polar oxide surfaces. *J. Phys.: Condens. Matter* **2000**, *12*, R367−R410.
(58) Saito, K.; Koga, K.; Kudo, A. Lithium niobate nanowires for photocatalytic water splitting. *Dalton Trans.* **2011**, *40*, 3909−3913.
(59) Yang, W.-C.; Rodriguez, B. J.; Gruverman, A.; Nemanich, R. J. Psolarization-dependent electron affinity of $LiNbO_3$ surfaces. *Appl. Phys. Lett.* **2004**, *85*, 2316−2318.
(60) Trasatti, S. The absolute electrode potential: an explanatory note. *Pure Appl. Chem.* **1986**, *58*, 955−966.

DOI: 10.1021/acsomega.8b03271
ACS Omega 2019, 4, 3850−3859